Encapsulated MWCNT@MOF-derived In_2S_3 tubular heterostructures for boosted visible-light-driven degradation of tetracycline

Yunhong Pi, Shuo Jin, Xiyi Li, Shi Tu, Zhong Li, Jing Xiao*

School of Chemistry and Chemical Engineering, and Guangdong Provincial Key Laboratory of Atmospheric Environment and Pollution Control, South China University of Technology, Guangzhou 510640, PR China

ABSTRACT

Constructing advanced heterojunction structures is an effective approach to improve light utility and enhance photogenerated charge separation and transfer for solar energy conversion. Herein, we reported a MWCNT@ MOF-derived In_2S_3 hollow tube heterostructure via facile MOF sulfidation process, significantly boosting its photocatalytic degradation performance of tetracycline (TC) under visible light irradiation. The MWCNT bonds to the In_2S_3 hollow tube strongly to construct an effective heterojunction, as illustrated in TEM and Raman spectroscopy. The 0.3%-MWCNT@MOF-derived In_2S_3 exhibited the highest photocatalytic activity for visible-light-driven TC degradation, achieving ~100% degradation efficiency, with its apparent reaction rate constants 3–5 times higher than that of the pure MOF-derived hollow In_2S_3 and traditional In_2S_3 bulk. The boosted visible-light-driven degradation efficiency was attributed to the synergy between electron acceptor of MWCNTs for enhanced separation of charge carriers and active center of MOF-derived In_2S_3 hollow tube with shorter transfer distance of charge carriers, which not only promotes the carrier transfer and inhibits the recombination rate effectively, but also improves the visible light response. Such MOF-derived visible-light-active heterostructures thus provide a novel insight into the development of highly efficient photocatalyst for a wide usage.

1. Introduction

Recent years have seen the raising of semiconductor-based photocatalytic procedure as one of the most promising technologies to address the environmental contamination issue, with its great potential in organic pollutants treatment [1–9]. From the viewpoint of solar energy utilization, it is desirable and urgent to develop highly active and environmental-friendly visible-light-driven photocatalysts to fulfill the increasing requirements of industrial applications [10,11]. Among all the visible-light-active photocatalysts, the metal sulfides (*e.g.*, In_2S_3, $ZnIn_2S_4$ and $CdIn_2S_4$) are intriguing ones with unique electronic structures (band gaps and redox potentials) and tunable optical properties [12–19], which make them as ideal candidates in photoredox catalysis, such as photocatalytic H_2 evolution reaction (HER) [12–14], CO_2 photoreduction [13,18] and organic photosynthesis [19]. Despite of these progresses, photo-stability and catalytic performance of single metal sulfide photocatalysts are still far from satisfactory, mainly due to the easy photo-corrosion, sluggish separation of electrons/holes and low migration kinetics of charge carriers [20].

Metal-organic frameworks (MOFs), constructed by metal-containing nodes and organic linkers through strong ionic bonding, have been demonstrated useful as photocatalysts like semiconductors when exposed to the light irradiation [21]. Based on the distinctive advantages of the structural regularity and synthetic tenability [22–24], MOFs are also widely employed as precursors to prepare functional materials with complex structures and tailored compositions (porous structures, single-shelled hollow structures, and multishelled hollow structures, *etc*) using the Ostwald ripening mechanism [25], such as metal oxides [26,27], metal sulfides [28–30], and porous carbon materials [31] for environmental and energy usage [32–35]. The resulting derivatives can not only form sophisticated morphology as well as unique structure, but also maintain high surface areas, rich active sites, and dispersed nanoscale subunits [36]. Lou et al. firstly employed MIL-68(In) as sacrificial precursor to synthesize hierarchical hollow In_2S_3-$CdIn_2S_4$ heterostructured nanotubes as efficient and stable photocatalysts for visible light CO_2 reduction [20]. Li et al. designed hollow ZnCdS rhombic dodecahedral cages based on ZIF-8 with high photocatalytic activity and recyclability for hydrogen evolution [36]. The hollow structures with interior cavity i) facilitates separation of charge carriers by decreasing diffusion length from bulk to surface, ii) offers large surface area to boost substrates adsorption and local concentration, and iii) promotes surface-dependent redox reactions on both sides of the

---

* Corresponding author.
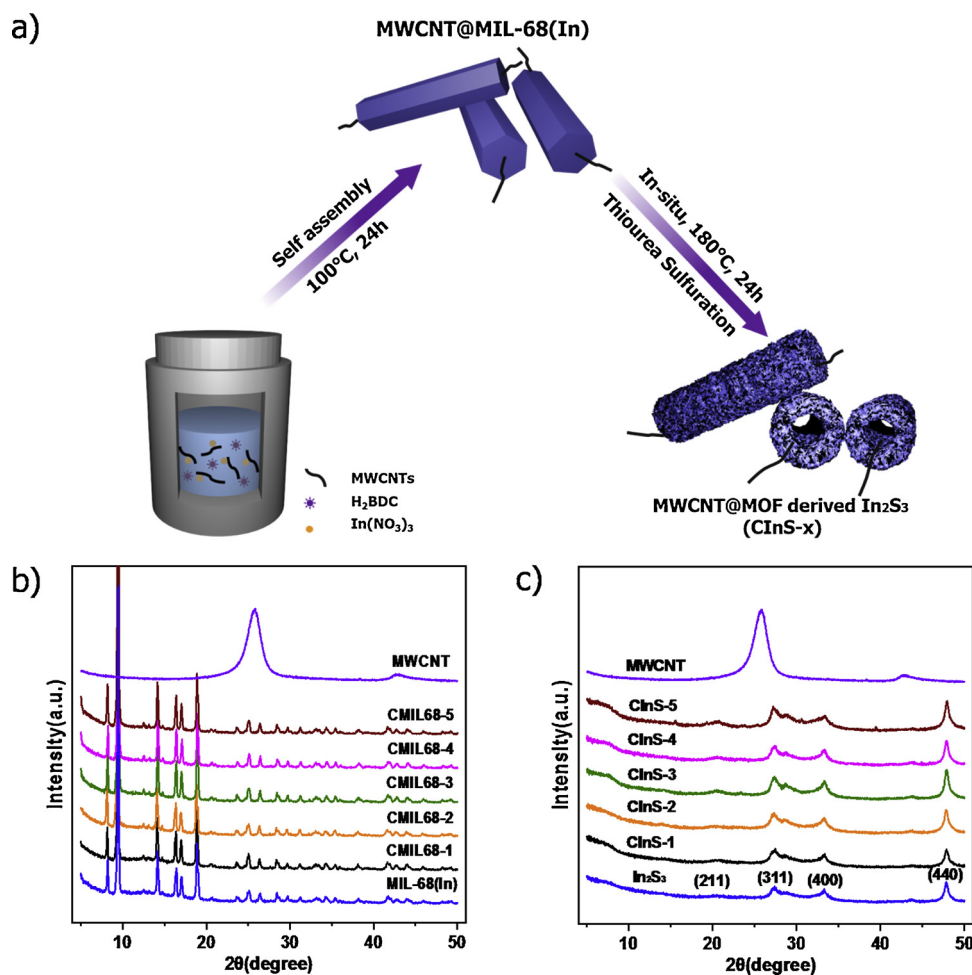*E-mail address:* cejingxiao@scut.edu.cn (J. Xiao).

Fig. 1. a) Illustration of the MWCNT@MOF-derived In_2S_3 photocatalyst synthesis; b) PXRD patterns of MWCNTs, MIL-68(In) and CMIL68-x composites; (c) PXRD patterns of MWCNTs, MOF-derived In_2S_3 and CInS-x composites.

shell [37–40]. Although the MOF-derived functional materials have a significant boost in recent years, the pristine merit of MOF as a platform to encapsulate diverse guests was often ignored during the derived process.

Owing to their excellent optical and electron transfer properties, carbon nanotubes (CNTs) have been widely studied to improve the photoactivity of semiconductors [41,42]. Based on our previous work which utilized multi-wall carbon nanotubes (MWCNTs) as electron acceptor to enhance the photoreduction performance of NH_2-MIL-68(In) platform [43], herein, rod-like MIL-68(In) is used beyond a platform to encapsulate MWCNTs but as a precursor for further sulfidation, resulting in a hollow-tube heterostructure of MWCNT@MOF derived In_2S_3. This novel heterostructure achieved the "one stone three birds" goal in photo-induced carriers: i) the hollow structures decreased the diffusion length of charge carriers from bulk to surface; ii) MWCNT was introduced as an electron acceptor to facilitate the separation of e^-/h^+; iii) the tube-like structure accelerates the migration kinetics of carriers. The enhanced photocatalytic performances were demonstrated through the degradation of tetracycline, which is a kind of persistent organic pollutants (POPs) in water under the visible light range [24]. Benefited from the optimized electronic structure and morphology, this hollow composite here remarkably outperformed traditional In_2S_3 bulk in both degradation kinetics and reusability.

2. Experimental section

2.1. Chemicals and reagents

Multiwalled carbon nanotube (MWCNT, 95%), Indium nitrate hydrate $(In(NO_3)_3 \cdot xH_2O, 99.99\%)$, and 1,4-benzenedicarboxylic acid (H_2BDC, 99%) were supplied by Aladdin. Nitric acid (HNO_3, 70% v/v), sulfuric acid (H_2SO_4, 70% v/v), monopotassium phosphate (KH_2PO_4, 99%), and phosphoric acid (H_3PO_4, 99%) were obtained from Alfa Aesar. Triethanolamine (TEOA), Benzoquinone (BQ), and isopropanol (IPA) were purchased from Sinopharm Chemical Reagent. *N*, *N*-dimethyl-formamide (DMF), ethanol (EtOH) and methanol (MeOH) were purchased from Guanghua Chemicals. All reagents and solvents were analytical grade.

2.2. Synthesis of MIL-68(In) and MOF-derived In_2S_3

According to a typical solvothermal method [44], MIL-68(In) was synthesized with an improved solvothermal process. First, 0.4082 g of $In(NO_3)_3 \cdot xH_2O$ and 0.2 g of H_2BDC were dissolved in 5 mL of DMF and stirred for 10 min. Subsequently, the clear solution was transferred into a 25 mL Teflon-lined stainless steel autoclave and heated at 100 °C for 24 h. After cooling to room temperature, the obtained white solid was collected and washed several times with DMF and immersed in anhydrous methanol for three days for guest molecules removal in the pores. Finally, the product was centrifuged and dried at 80 °C overnight.

For synthesis of In_2S_3 nanotubes derived from In-MOF, 100 mg of

the above-obtained MIL-68(In) hexagonal precursors were added into 15 mL of an ethanol solution containing 300 mg of thiourea, and stirred for 10 min. Then, the resultant mixture was transferred into a 100 mL Teflon-lined autoclave and maintained at 180 °C for 24 h. After cooling down to room temperature, the saffron yellow precipitate was filtrated and washed with ethanol and H_2O three times, and immersed in anhydrous methanol for two days to remove excess unreacted thiourea before the hollow In_2S_3 nanotube was obtained.

2.3. Synthesis of MWCNT@MIL-68(In) CMIL-68-x and MWCNT@MOF-derived In_2S_3 CInS-x

Before MWCNT was employed, the raw MWCNTs should be purified and surface functionalized first according to a reported procedure [45]. For synthesis of MWCNT@MIL-68(In), a pre-determined weight percentage of surface functionalized MWCNT as 0.1%, 0.3%, 0.5%, 1.0%, and 5.0% were first introduced into 5 mL of DMF containing 0.4082 g of $In(NO_3)_3 \cdot xH_2O$ (0.4082 g) and stirred for 12 h until a uniform mixture was achieved. Subsequently, with H_2BDC (0.2 g) being added to the above mixture and sonicated for 10 min, the resulting suspension went through the same solvothermal procedure and purification process as previously employed for MIL-68(In). The resulting MWCNT@MIL-68(In) as CMIL68-x (x = 1, 2, 3, 4, 5) composites were subjected to the same sulfidation procedure as that of In_2S_3 to yield the MWCNT@MOF-derived In_2S_3(CInS-1, CInS-2, CInS-3, CInS-4, and CInS-5, respectively). The synthetic route to MWCNT@MOF-derived In_2S_3 encapsulation tubular heterostructures is schematically illustrated in Fig. 1a. And the final contents of MWCNTs in the CInS-x composites are calculated to be 0.83, 4.37, 6.83, 7.82 and 17.45 wt% respectively from TG analysis (**Figure S1**, Table S1, Supporting Information).

2.4. Characterization methods

Powder X-ray diffraction (PXRD) study was performed using a Bruker D8 Advance diffractometer with monochromatized Cu Kα radiation ($\lambda = 0.15418$ nm) source at 40 kV and 40 mA. The Fourier-transform infrared (FTIR) spectroscopy measurements were conduct with Nicolet 6700 FTIR Spectrometric Analyzer using KBr pellets. The morphological study of the as-synthesized hybrid nanostructures was obtained through Scanning electron microscope (SEM), transmission electron microscopy (TEM) and corresponding quantitative energy dispersive X-ray spectroscopy (EDS). Raman spectra were conduct on a LabRAM Aramis, T64000 model, exciting the samples by a 525 nm laser beam. The interaction and chemical compositions of the composites were analysed by X-ray photoelectron spectroscopy (XPS, ESCALAB 250Xi). UV–Vis diffused reflectance spectra (DRS) were carried out on a UV–Vis spectrophotometer (UV-3600, Shimadzu, Japan), with $BaSO_4$ as a reflectance standard. The photoluminescence spectra (PL) were observed on a fluorescence spectrometer (Hitachi F-4600) with an excitation wavelength of 400 nm. Electron Paramagnetic Resonance (EPR) spectra was achieved on Japanese electronics (JEOL) JES FA200. The EPR signals of radicals trapped by trap reagent DMPO (5, 5′- dimethyl-1-pirroline-*N*-oxide) (Sigma Chemical Co.) in methanol were examined with a spot UV–Vis light source (420 nm UV-cutoff filter) in situ by every 5 min under irradiation. MS was conducted in an electrochemical work station (CHI660D Instruments) connected to a computer.

2.5. Evaluation of photocatalytic performance

The photocatalytic activity of hollow MWCNT@MOF-derived In_2S_3 composites CInS-x were tested by the photocatalytic decomposition of TC with visible light illumination (λ > 420 nm) after adsorption process. A 300 W Xenon lamp with a 420 nm cutoff filter was used as the visible light source (20 cm far away from the photocatalytic reactor with light intensity about 25 mW/cm^2). 15 mg of the as-prepared

photocatalyst was dispersed in 50 mL of TC aqueous solution with the initial concentration of 30 mg/L in a 50 mL cylindrical Pyrex reactor. After being stirred in dark for 2 h to achieve adsorption/desorption equilibrium, the suspensions were irradiated in open air at room temperature, without addition of H_2O_2. About 2 mL of suspension was withdrawn regularly and filtered through 0.22 μm PTFE syringe filters for HPLC analysis, which comprised an XBridge column (4.6 × 250 mm, C18, 5 μm) and an UV–Vis detector. Methanol and 0.05 M KH_2PO_4 buffer solution acidified at pH = 3 with H_3PO_4 were used as mobile phases A and B ($v_A/v_B = 25/75$), respectively, at a flow rate of 0.8 mL·min^{-1}. The oven temperature was maintained at 40 °C. The detector wavelength was set at 375 nm and the injection volume was 10 μL. To determine the extent of mineralization, total organic carbon (TOC) contents of solution were measured with a Shimadzu TOC-VCPH/CPN analyzer. All the photocatalytic result measurements mentioned were repeated twice to ensure the reliability of the results. After photocatalytic reaction, the catalyst was collected and recovered for recycle tests.

3. Results and discussion

3.1. Characterizations

The crystalline phase and morphology of the obtained samples were studied by PXRD (Fig. 1**b-c**), SEM (Fig. 2), and high-resolution transmission electron microscope (HRTEM) (**Figure S2,** Supporting Information). From the PXRD analysis (Fig. 1b), the diffraction patterns of the composites CMIL-68-x (x = 1–5) were in good agreement with that of the MIL-68(In) [44]. After sulfidation at 180 °C for 24 h, the prominent peaks of MIL-68(In) completely disappeared, and converted into cubic In_2S_3 phase (JCPDS no. 32-0456) without detectable impurities (Fig. 1c). The similar diffraction peaks at 21.0°, 27.6°, 32.7° and 48.2° are obvious in both the In_2S_3 and the composite, corresponding to the (211), (311), (400) and (440) of β-In_2S_3, respectively [46,47]. Nevertheless, the typical diffraction peaks of MWCNT was absent in both kind of composites, which can be attributed to the low content and highly dispersion of MWCNTs in the composites [48].

Such conversion was further supported by the morphology characterization with SEM. As shown in Fig. 2**a-b**, the surface of MIL-68(In) hexagonal micro-rods were smooth with the average length and diameter of 20 μm and 500 nm, respectively, while after complete sulfidation, the as-obtained In_2S_3 showed rather rough surface and hollow nanotube structures appeared (Fig. 2**c-d**). In the meantime, the as-obtained composites well inherited the one-dimensional (1D) morphology from their MIL-68(In) precursors with 300–400 nm in width and 18–20 μm in length. Interestingly, the MWCNTs were distributed along the hollow nanotube wall and pass through the nanotube, as demonstrated in Fig. 2**d**. Besides, TEM images revealed the well-defined hollow In_2S_3 nanotubes with MWCNTs passing through, and also HRTEM images displayed a clear crystal lattice spacing of 2.69 nm, which was well matched with the (400) plane of cubic In_2S_3 (Fig. 3**a-b**). Furthermore, the elemental mapping results showed uniform dispersion of In, S, C and O over the whole hollow heterojunction structure (Fig. 3**c-f**). All these results confirmed the successful construction of MWCNT@MOF-derived In_2S_3 heterostructures.

Raman spectroscopy was carried out to confirm the presence of MWCNT in the nanocomposites and its interaction with In_2S_3. As shown in Fig. 4a, two obvious peaks are found to be located at 1333 and 1592 cm^{-1}, corresponding to the typical D and G bands of MWCNT, respectively [49]. Notably, the D band of MWCNT upshifts from 1333 to 1350 cm^{-1} in the CInS-2 composite, which can presumably be attributed to the bonding interaction between hollow In_2S_3 and MWCNT, indicating the integration of MWCNT into the In_2S_3 as well as the electron density spill from In_2S_3 to MWCNT. The interaction between the In_2S_3 and MWCNT was further supported by X-ray photoelectron spectroscopy (XPS). As shown in Fig. 4b, two peaks at 452.3 and
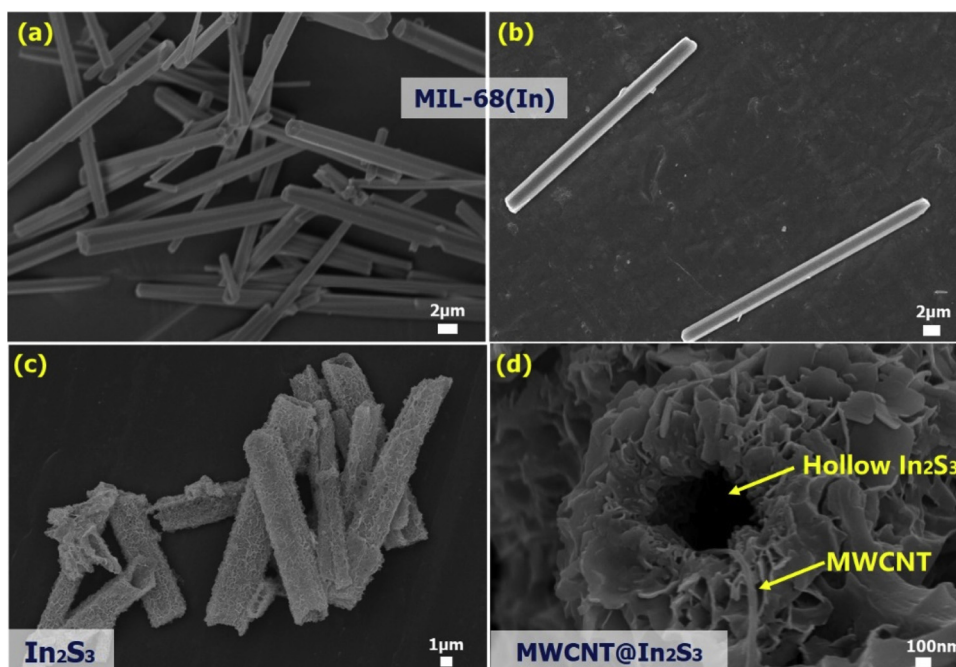
Fig. 2. SEM images of a–b) MIL-68(In), c) MOF-derived In_2S_3, and d) MWCNT@MOF-derived In_2S_3 composite.

444.8 eV were assigned to In $3d_{3/2}$ and In $3d_{5/2}$, indicating the exclusive existence of In^{3+} [50]. Noteworthy, the binding energies of In $3d_{3/2}$ and In $3d_{5/2}$ of the composite CInS-2 slightly downshift to 452.1 and 444.6 eV by 0.2 eV compared to pure In_2S_3, indicating the increase in the electronic density of In^{3+} [51,52] after combining with MWCNT due to the surrounded π-rich conjugation structures of MWCNT [53]. Additionally, the survey spectrum also gives the signal peaks of C, O, In and S elements, displaying the specific element contents in photocatalysts (Table S2).

The optical respond of the materials varied significantly due to the incorporation of MWCNT, as suggested in Fig. 4c. From the UV–Vis diffuse reflectance spectra (DRS), it should be noted that the adsorption edge of In_2S_3 derived from MOF extended to 650 nm, which is longer than that of previous reported (575 nm) [54], indicating the improved solar energy utility of hollow nanotube structures. For bare MWCNT, it exhibited strong light absorption in the range of 200–800 nm,

consistent with the literature report [55]. After the introduction of MWCNT, both the red-shifts and enhanced visible light adsorptions were observed for the CInS-x composites, demonstrating the band-gap narrowing of the CInS-x composites and potential improvement of photo-activity. It can also be confirmed through the intercepts of the tangents of $(Ahv)^{1/2}$ vs. photo energy of the CInS-x composites, as shown in the inset of Fig. 4c. The corresponding band-gaps were estimated to be 1.78, 1.74, 1.58, 1.60, 1.64, and 1.45 eV for In_2S_3, CInS-1, CInS-2, CInS-3, CInS-4, and CInS-5, respectively.

3.2. Photocatalytic performance

To evaluate the photocatalytic performance of CInS-x samples, tetracycline (TC) was selected as a representative organic pollutant for photocatalytic degradation under visible light irradiation. As clearly exhibited in Fig. 5a, MIL-68(In) MOF only displayed 18.5% of TC
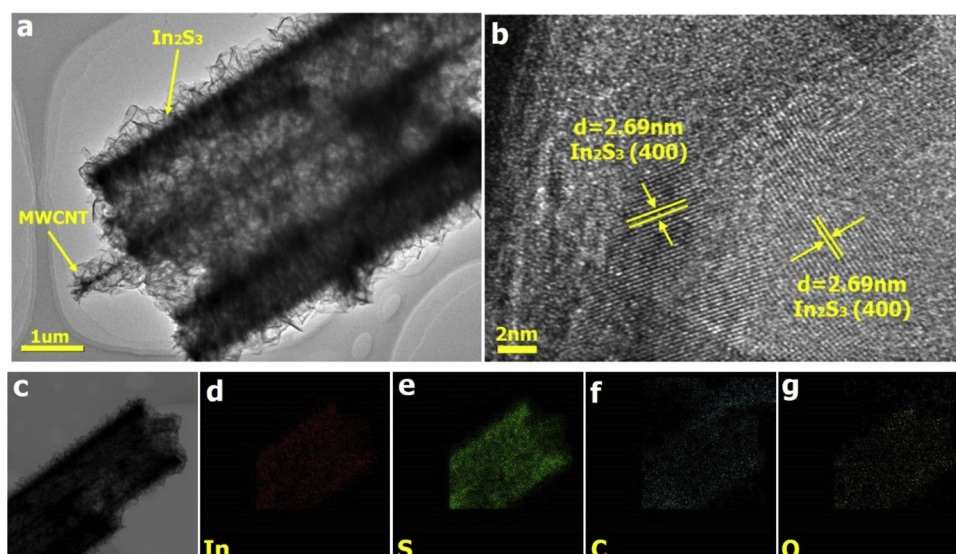

Fig. 3. a, c–g) TEM images of CInS-2 and corresponding quantitative EDS mapping of d) In, e) S, f) C and g) O; b) HRTEM images of CInS-2.
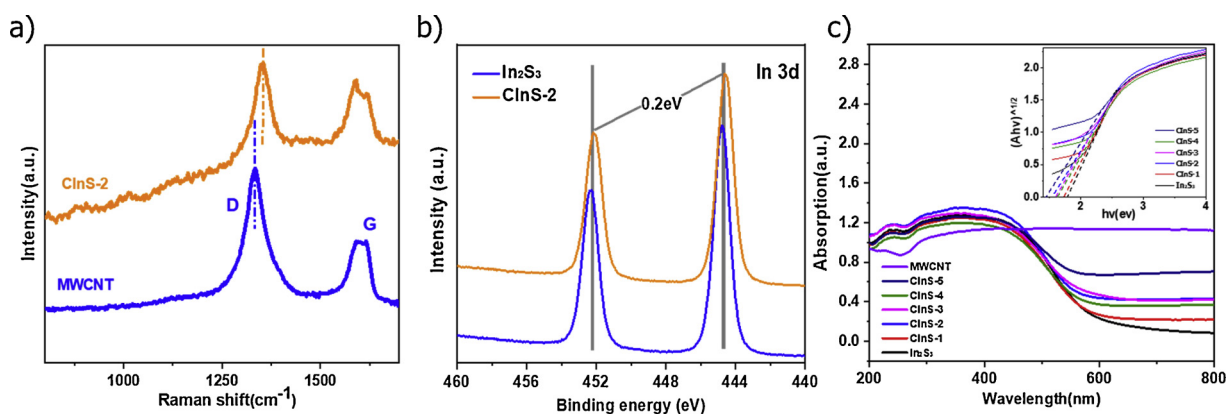
Fig. 4. a) Raman spectra of MWCNT and CInS-2 composite; b) In 3d XPS spectra of MOF-derived In_2S_3 and CInS-2 composite; c) The UV–Vis DRS spectra and plots of $(Ahv)^{1/2}$ vs. photon energy of MOF-derived In_2S_3 and MWCNT@ MOF-derived In_2S_3 composite CInS-x (x = 1–5) and MWCNT.

degradation efficiency after 120 min irradiation, and 47.1% of photocatalytic performance was observed using traditional In_2S_3 synthesized according to the previous reported work [56]. However, the hollow In_2S_3 derived from MIL-68(In) displayed superior photo-activity, up to 61.7% within 120 min. More importantly, the photocatalytic performance was significantly enhanced with MWCNT incorporated into the MOF-derived In_2S_3 (CInS-x, x = 1–5), and CInS-2 with 0.3% MWCNT exhibited the highest degradation rate which could reach 100% within 120 min. Further increasing the amount of MWCNT resulted in decreasing in the photocatalytic activity, which may be ascribed to the

"covering effect": i) excessive MWCNT might cover the surface active sites of In_2S_3; ii) the overloaded MWCNT might shield light absorption by In_2S_3 and thus decrease the photo-induced electrons [57]. However, all these photocatalysts displayed much higher efficiency than commercial P25, with only 23.1% of TC degradation under the same condition (**Figure S2**). To further reveal the environment fate of antibiotic over CInS-x composite photocatalysts, the extent of mineralization is quantified by the decrease of TOC concentration (Fig. 5b). For CInS-2, about 55.2% of total organic carbon in TC solution is mineralized after 120 min irradiation, which is significantly higher than those of hollow
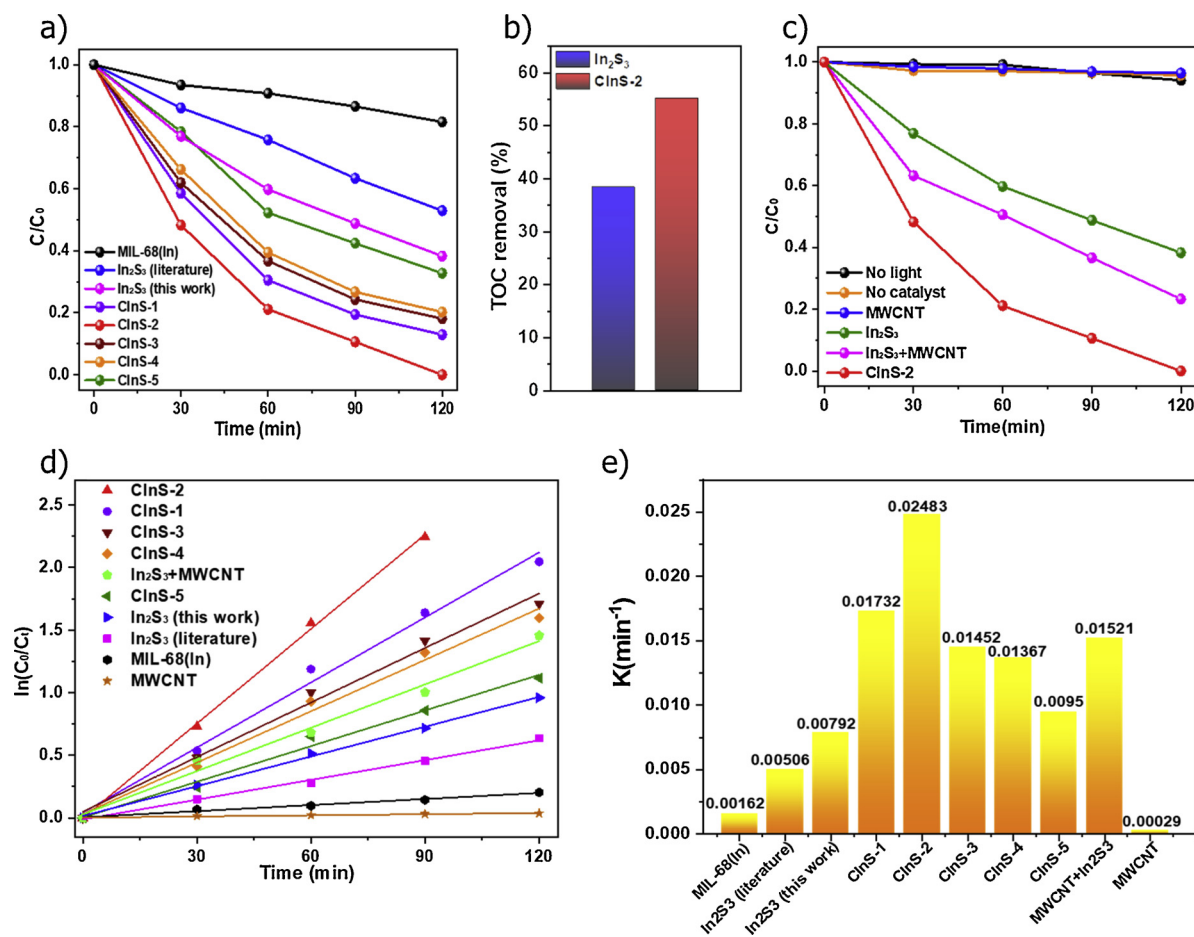

Fig. 5. a) Photodegradation efficiency of TC over the MIL-68(In), In_2S_3 (literature), MOF-derived In_2S_3 (this work) and CInS-x(x = 1–5); b) TOC removal efficiency of TC by hollow In_2S_3 and CInS-2; c) Photodegradation efficiency of TC under different conditions; d) Pseudo-first-order kinetics curves of the degradation of TC under different conditions; e) Comparison of the apparent reaction rate constants of the TC degradation using different photocatalysts.

In_2S_3 photocatalyst (38.4%), further indicating the enhanced photocatalytic and mineralization performance of hollow In_2S_3 with MWCNT modification.

Control experiments were carried out to further study the outstanding photocatalytic activity of the CInS-2 composite. Fig. 5c exhibited the variation of TC concentration (C/C_0) over time at various conditions. After being irradiated with visible light for 120 min, the TC concentration displayed nearly no change without adding photocatalysts. Experiment with MWCNT itself showed slight decrease of TC concentration, which can be attributed to the adsorption of TC by MWCNT. Almost no obvious decrease was observed under dark condition even with photocatalyst, suggesting the catalytic TC degradation as a photo-induced process using the CInS-2 acted as photocatalyst. It should also be marked that CInS-2 composite showed much higher TC photoreduction efficiency than the physical mixture of hollow In_2S_3 and MWCNT, emphasizing that the close interaction between MWCNT and In_2S_3 in CInS-2 composite made pronounced effect on TC photodegradation. Additionally, Fig. 5d displayed the kinetic fitting curves of $ln(C/C_0)$ over irradiation time, fitting well with the pseudo-first-order rate equation. And obviously in Fig. 5e, the kinetic rate constant of CInS-2 ($0.02483\,min^{-1}$) tripled that of MOF-derived In_2S_3 (this work, $0.00792\,min^{-1}$), indicating the incorporation of MWCNT played a significant role in the dramatically enhanced photodegradation kinetics.

From the viewpoint of practical application, it is of significant importance to investigate the reusability and stability (water stability and photo stability) of photocatalytic materials. The stability of CInS-2 was confirmed in the recycling experiments, where CInS-2 was regenerated through simple filtration and washed with DI water and ethanol for several times, and then dried at 60 °C before reuse. As shown in Fig. 6a, after three successive degradation runs, obviously, less degradation efficiency decrease was observed for CInS-2 composite, much better photo-activity was maintained than that of pure In_2S_3 derived from MOF, with apparent reaction rate constant nearly eight times higher after three cycles. The detection of In species leaching during the photocatalytic degradation was conducted by ICP-AES. The results revealed much lower In species leaching in the post-reaction solution of CInS-2 ($1.49 \times 10^{-9}\,mol\,mL^{-1}$) than that in In_2S_3 ($2.31 \times 10^{-9}\,mol\,mL^{-1}$), as shown in Table S3. Although the photo corrosion always happens inevitably in sulfide [20], the introduction of MWCNT indeed enhance the stability of photocatalysts, including the structure and the performance. The stability of CInS-2 composite was also revealed by the PXRD analysis (Fig. 6b), which showed no obvious changes after the photoreaction. These results well illustrated the outstanding reusability and robustness of CInS composite, and the incorporation of MWCNT

into MOF-derived In_2S_3 can act as an effective method to improve the stability from which metal sulfides are usually suffering [58].

3.3. Illustration of photocatalytic mechanism

To further investigate the underlying mechanism behind the excellent photocatalytic activities of MWCNT@ MOF-derived In_2S_3 composite CInS-2, active species trapping experiments were carried out. Specifically, triethanolamine (TEOA), benzoquinone (BQ), and isopropanol (IPA) were employed as the scavengers of holes (h^+), superoxide radicals ($\cdot O_2^-$) and hydroxyl radicals ($\cdot OH$), respectively [59]. Fig. 7a illustrated the active species trapping experiments in photocatalytic degradation of TC with CInS-2. The results showed that while the addition of IPA only slightly interfered with the photocatalytic activity, the presence of TEOA or BQ largely suppressed the photocatalytic degradation efficiency of TC. Thus, it could be inferred that h^+ and $\cdot O_2^-$ were the main active species in the TC photodegradation process with MWCNT@ MOF-derived In_2S_3 composite.

The prolonged electron life time in the composite should be attributed to the decrease in the recombination of the electron–hole pairs, as supported by the steady-state photoluminescence (PL) spectra. As shown in Fig. 7b, the PL intensity in the composite was remarkably quenched compared with pure MOF-derived hollow In_2S_3, demonstrating that the combining of In_2S_3 and MWCNT could retard the charge recombination, and thus the charge carriers generated by In_2S_3 are favorably transferred to the electron acceptors (MWCNT) [60]. To further investigate the effect of MWCNT modification on the band structures of CInS-x, the flat-band potentials (E_{FB}) of In_2S_3 and CInS-2 were measured separately by performing the typical Mott-Schottky measurements. Mott-Schottky plots of In_2S_3 and CInS-2 were shown in Fig. 7c and Figure S3 respectively, revealing their typical n-type semiconductivity because of the positive slope [61,62]. For n-type semiconductors, their conduction band potential (E_{CB}) are very close to the E_{FB} [63]. Therefore, the E_{CB} deduced from Mott-Schottky plots are about -0.30 and $-0.28\,eV$ vs. Ag/AgCl (-0.08 and $-0.06\,eV$ vs. NHE) for In_2S_3 and CInS-2, respectively. Apparently, the conduction band edge potential of CInS-2 showed a positive shift in comparison with In_2S_3. With the bandgap values of In_2S_3 and CInS-2 estimated from the UV–Vis DRS spectrum (Fig. 4 inset), the calculated valence band potentials (E_{VB}) are 1.70 and 1.52 eV vs. NHE, respectively.

Based on the above experimental results, the enhanced photodegradation mechanism of TC over the MWCNT@ MOF-derived In_2S_3 heterojunction is proposed in Scheme 1. Under visible light illumination, the electrons were first readily excited from valence band (VB) to conduction band (CB) in In_2S_3, generating the photo-induced
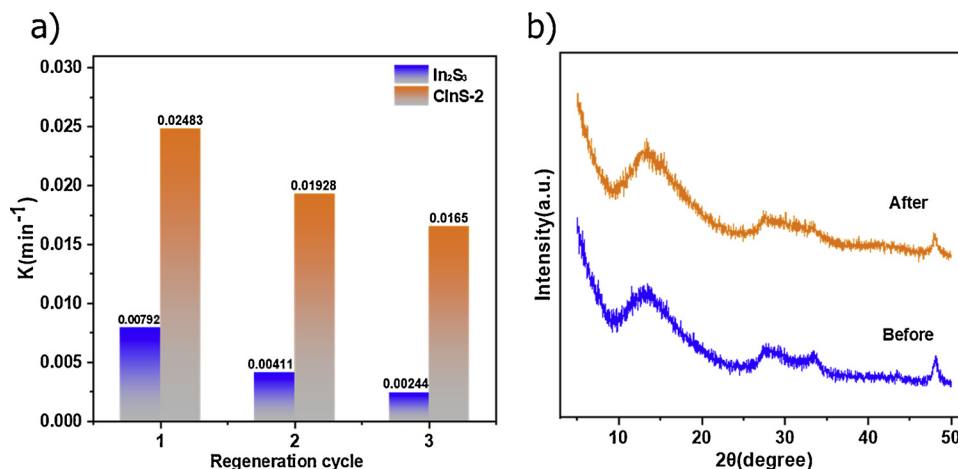

Fig. 6. a) Apparent reaction rate constants of TC degradation over MOF-derived In_2S_3 and CInS-2 at multiple regeneration cycles; b) PXRD pattern of CInS-2 before and after photodegradation of TC under visible light irradiation.
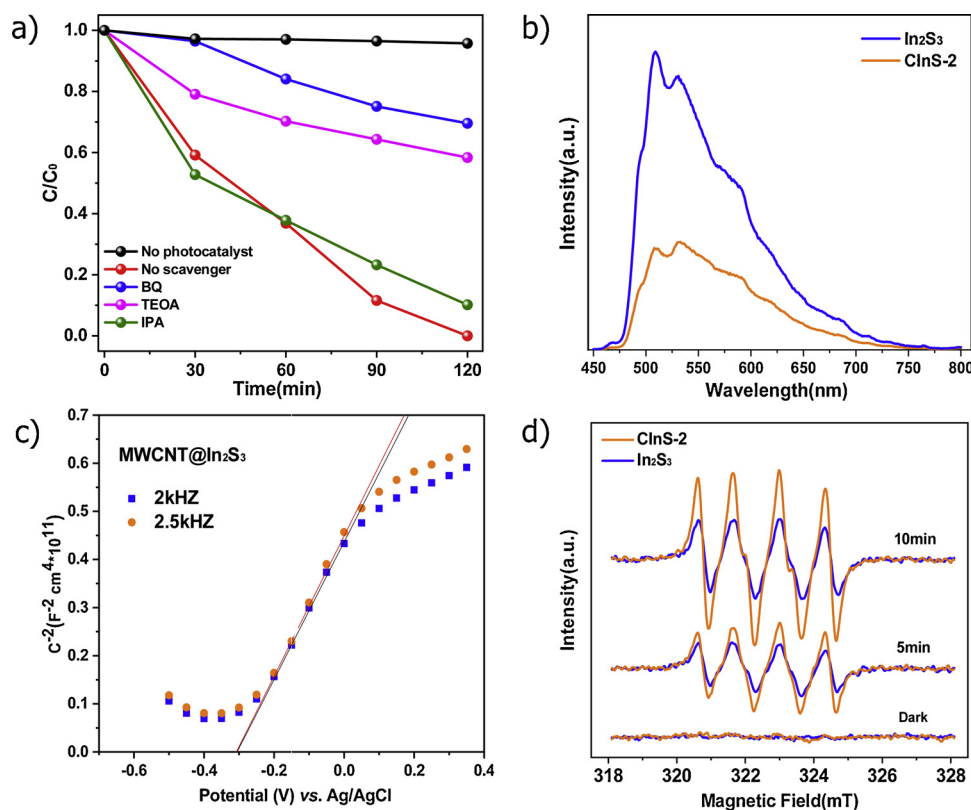
Fig. 7. a) Kinetic curves of CInS-2 on the degradation of TC in the presence of different radical scavengers under visible light irradiation; b) The PL spectra of MOF-derived In_2S_3 and CInS-2; c) Mott-Schottky plots of CInS-2 at different frequency; d) ESR spectra of DMPO–•O_2^- adducts formed with irradiation time of visible light in the suspension of MOF-derived In_2S_3 and CInS-2.

electron–hole pairs. The incorporated MWCNT served as excellent photosensitizer to enhance light harvesting as well as electron acceptor to induce the photogenerated electron transfer. Therefore, the photogenerated electrons in hollow In_2S_3 could easily migrate to the MWCNT, facilitating charge transfer and retarding e^-/h^+ recombination, thus providing an enhanced photocatalytic activity. More importantly, the superoxide radical anions generated in the hollow In_2S_3 and CInS-2 were measured by electron spin resonance (ESR) spectroscopy using 5,5-dimethyl-1-pyrroline-*N*-oxide (DMPO) as a probe. As shown in Fig. 7d, no obvious ESR signal was detected in the dark, whereas the characteristic signals of DMPO–$^.O_2^-$ species appeared in both samples after irradiation [64]. Notably, compared with MOF-derived In_2S_3, CInS-2 showed significant higher intensity of DMPO–$^.O_2^-$,

indicating a much more efficient formation of $^.O_2^-$ in the MWCNT@ MOF-derived In_2S_3 system [65]. Hence, the above results inferred that in the photodegradation of TC, the e^- transferred from CB to MWCNT activated the O_2 to generate $^.O_2^-$ as true active species, and on the other hand, the h^+ left in VB of In_2S_3 directly induced the photo-oxidation of TC. (Scheme 1)

4. Conclusions

In summary, we successfully designed and fabricated the MWCNT@ MOF-derived In_2S_3 hollow tube heterostructures by a facile sulfidation process. Such heterostructural photocatalyst displayed a remarkably boosted visible-light driven photocatalytic degradation performance of

MWCNT@MOF derived In₂S₃
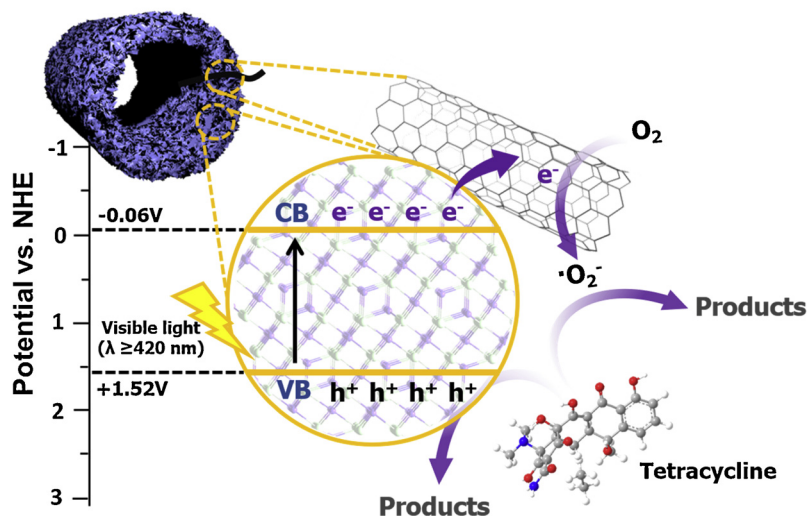
Scheme 1. Proposed mechanism for TC photodegradation with MWCNT@ MOF-derived In_2S_3 composite under visible light.

TC compared with pure hollow In_2S_3, and the MWCNT content in the composite was optimized to be 4.37% (CInS-2) to display the best activity. Systematical studies proved that the coactions of the MOF-derived In_2S_3 and MWCNT in such a hollow hierarchical way significantly increased the light utility in the visible region and facilitated the separation of the photo-induced electron–hole pairs. Mechanism studies revealed that the boosted visible-light driven photocatalytic degradation of the MWCNT@MOF-derived In_2S_3 composite was derived from the formation of MWCNT@ MOF-derived In_2S_3 heterojunction that facilitates the generation of the $\cdot O_2^-$, and the degradation reaction occurred through the synergetic effect of $\cdot O_2^-$ and h^+ both generated in the system. We believed that such unique and successful attempt to construct heterostructures in MOF-derived visible light active materials for performance enhancement will largely promote the design and development of applicable photocatalysts.

Conflict of interest

The authors declare no conflict of interest.

Acknowledgments

Appendix A. Supplementary data

Supplementary material related to this article can be found, in the online version, at doi:https://doi.org/10.1016/j.apcatb.2019.117882.

References

[1] Z. Yi, J. Ye, N. Kikugawa, T. Kako, S. Ouyang, H. Stuart-Williams, H. Yang, J. Cao, W. Luo, Z. Li, Y. Liu, R.L. Withers, An orthophosphate semiconductor with photo-oxidation properties under visible-light irradiation, Nat. Mater. 9 (2010) 559–564.

[2] S. De, A.M. Balu, J.C. vander Waal, R. Luque, Biomass-derived porous carbon materials: synthesis and catalytic applications, ChemCatChem 7 (2015) 1608–1629.

[3] H. Wang, L. Zhang, Z. Chen, J. Hu, S. Li, Z. Wang, J. Liu, X. Wang, Semiconductor heterojunction photocatalysts: design, construction, and photocatalytic performances, Chem. Soc. Rev. 43 (2014) 5234–5244.

[4] D.J. Martin, G. Liu, S.J. Moniz, Y. Bi, A.M. Beale, J. Ye, J. Tang, Efficient visible driven photocatalyst, silver phosphate: performance, understanding and perspective, Chem. Soc. Rev. 44 (2015) 7808–7828.

[5] H.S. Jung, Y.J. Hong, Y. Li, J. Cho, Y.-J. Kim, G.-C. Yi, Photocatalysis using GaN nanowires, ACS Nano 2 (2008) 637–642.

[6] J. Chen, G. Li, Y. Huang, H. Zhang, H. Zhao, T. An, Optimization synthesis of carbon nanotubes-anatase TiO_2 composite photocatalyst by response surface methodology for photocatalytic degradation of gaseous styrene, Appl. Catal. B Environ. 123–124 (2012) 69–77.

[7] W. Zhang, G. Li, H. Liu, J. Chen, S. Ma, T. An, Micro/nano-bubble assisted synthesis of $Au/TiO_2@CNTs$ composite photocatalyst for photocatalytic degradation of gaseous styrene and its enhanced catalytic mechanism, Environ. Sci. Nano 6 (2019) 948–958.

[8] P. Wei, D. Qin, J. Chen, Y. Li, M. Wen, Y. Ji, G. Li, T. An, Photocatalytic ozonation mechanism of gaseous n-hexane on $MOx–TiO_2$–foam nickel composite (M = Cu, Mn, Ag): unveiling the role of $\cdot OH$ and $\cdot O_2^-$, Environ. Sci. Nano 6 (2019) 959–969.

[9] Y. Wang, D. Yang, S. Li, M. Chen, L. Guo, J. Zhou, Ru/hierarchical HZSM-5 zeolite as efficient bi-functional adsorbent/catalyst for bulky aromatic VOCs elimination, Microporous Mesoporous Mater. 258 (2018) 17–25.

[10] W.-J. Ong, L.-L. Tan, Y.H. Ng, S.-T. Yong, S.-P. Chai, Graphitic carbon nitride (g-C_3N_4)-Based photocatalysts for artificial photosynthesis and environmental remediation: are we a step closer to achieving sustainability? Chem. Rev. 116 (2016) 7159–7329.

[11] Y. Li, K. Lv, W. Ho, F. Dong, X. Wu, Y. Xia, Hybridization of rutile TiO_2 ($rTiO_2$) with g-C_3N_4 quantum dots (CN QDs): an efficient visible-light-driven Z-scheme hybridized photocatalyst, Appl. Catal. B Environ. 202 (2017) 611–619.

[12] K. Iwashina, A. Iwase, Y.H. Ng, R. Amal, A. Kudo, Z-schematic water splitting into

[13] H_2 and O_2 using metal sulfide as a hydrogen-evolving photocatalyst and reduced graphene oxide as a solid-state Electron mediator, J. Am. Chem. Soc. 137 (2015) 604–607.

[13] X. Jiao, Z. Chen, X. Li, Y. Sun, S. Gao, W. Yan, C. Wang, Q. Zhang, Y. Lin, Y. Luo, Y. Xie, Defect-mediated Electron–Hole separation in one-unit-Cell $ZnIn_2S_4$ layers for boosted solar-driven CO_2 reduction, J. Am. Chem. Soc. 139 (2017) 7586–7594.

[14] B.B. Kale, J.-O. Baeg, S.M. Lee, H. Chang, S.-J. Moon, C.W. Lee, $CdIn_2S_4$ Nanotubes and "Marigold" Nanostructures: A Visible-Light Photocatalyst, Adv. Funct. Mater. 16 (2006) 1349–1354.

[15] W. Chen, Y.-X. Hua, Y. Wang, T. Huang, T.-Y. Liu, X.-H. Liu, Two-dimensional mesoporous g-C_3N_4 nanosheet-supported $MgIn_2S_4$ nanoplates as visible-light-active heterostructures for enhanced photocatalytic activity, J. Catal. 349 (2017) 8–18.

[16] S.K. Batabyal, S.E. Lu, J.J. Vittal, Synthesis, characterization, and photocatalytic properties of In_2S_3, $ZnIn_2S_4$, and $CdIn_2S_4$ nanocrystals, Cryst. Growth Des. 16 (2016) 2231–2238.

[17] S.K. Apte, S.N. Garaje, R.D. Bolade, J.D. Ambekar, M.V. Kulkarni, S.D. Naik, S.W. Gosavi, J.O. Baeg, B.B. Kale, Hierarchical nanostructures of $CdIn_2S_4$ via hydrothermal and microwave methods: efficient solar-light-driven photocatalysts, J. Mater. Chem. 20 (2010) 6095–6102.

[18] A. Iwase, S. Yoshino, T. Takayama, Y.H. Ng, R. Amal, A. Kudo, Water splitting and CO_2 reduction under visible light irradiation using Z-Scheme systems consisting of metal sulfides, $CoOx$-Loaded $BiVO_4$, and a reduced graphene oxide electron mediator, J. Am. Chem. Soc. 138 (2016) 10260–10264.

[19] X. Gou, F. Cheng, Y. Shi, L. Zhang, S. Peng, J. Chen, P. Shen, Shape-controlled synthesis of ternary chalcogenide $ZnIn_2S_4$ and $CuIn(S,Se)_2$ nano-/Microstructures via facile solution route, J. Am. Chem. Soc. 128 (2006) 7222–7229.

[20] S. Wang, B.Y. Guan, Y. Lu, X.W.D. Lou, Formation of hierarchical In_2S_3–$CdIn_2S_4$ heterostructured nanotubes for efficient and stable visible light CO_2 reduction, J. Am. Chem. Soc. 139 (2017) 17305–17308.

[21] C.G. Silva, A. Corma, H. García, Metal–organic frameworks as semiconductors, J. Mater. Chem. 20 (2010) 3141–3156.

[22] Y. Liu, S.-Y. Moon, J.T. Hupp, O.K. Farha, Dual-function metal–Organic framework as a versatile catalyst for detoxifying chemical warfare agent simulants, ACS Nano 9 (2015) 12358–12364.

[23] C. Duan, F. Li, L. Li, H. Zhang, X. Wang, J. Xiao, H. Xi, Hierarchically structured metal–organic frameworks assembled by hydroxy double salt–template synergy with high space–time yields, CrystEngComm 20 (2018) 1057–1064.

[24] Y. Pi, X. Li, Q. Xia, J. Wu, Y. Li, J. Xiao, Z. Li, Adsorptive and photocatalytic removal of Persistent Organic Pollutants (POPs) in water by metal-organic frameworks (MOFs), Chem. Eng. J. 337 (2018) 351–371.

[25] Z. Hua Chun, Ostwald ripening: a synthetic approach for hollow nanomaterials, Curr. Nanosci. 3 (2007) 177–181.

[26] H. Hu, B. Guan, B. Xia, X.W. Lou, Designed formation of $Co_3O_4/NiCo_2O_4$ double-shelled nanocages with enhanced pseudocapacitive and electrocatalytic properties, J. Am. Chem. Soc. 137 (2015) 5590–5595.

[27] R. Li, L. Sun, W. Zhan, Y.-A. Li, X. Wang, X. Han, Engineering an effective noble-metal-free photocatalyst for hydrogen evolution: hollow hexagonal porous micro-rods assembled from $In_2O_3@carbon$ core–shell nanoparticles, J. Mater. Chem. A Mater. Energy Sustain. 6 (2018) 15747–15754.

[28] J. Nai, J. Zhang, X.W.D. Lou, Construction of single-crystalline Prussian blue analog hollow nanostructures with tailorable topologies, Chem 4 (2018) 1967–1982.

[29] P. Zhang, S. Wang, B.Y. Guan, X.W. Lou, Fabrication of CdS hierarchical multi-cavity hollow particles for efficient visible light CO_2 reduction, Energy Environ. Sci. 12 (2019) 164–168.

[30] Q. Mao, J. Chen, H. Chen, Z. Chen, J. Chen, Y. Li, Few-layered $1T$-MoS_2-modified ZnCoS solid-solution hollow dodecahedra for enhanced photocatalytic hydrogen evolution, J. Mater. Chem. A 7 (2019) 8472–8484.

[31] B.Y. Guan, L. Yu, X.W.D. Lou, A dual-metal–organic-framework derived electrocatalyst for oxygen reduction, Energy Environ. Sci. 9 (2016) 3092–3096.

[32] Y. Si, M. Chen, L. Wu, Syntheses and biomedical applications of hollow micro-/nano-spheres with large-through-holes, Chem. Soc. Rev. 45 (2016) 690–714.

[33] Y.-Z. Zhang, Y. Wang, Y.-L. Xie, T. Cheng, W.-Y. Lai, H. Pang, W. Huang, Porous hollow Co_3O_4 with rhombic dodecahedral structures for high-performance supercapacitors, Nanoscale 6 (2014) 14354–14359.

[34] H. Liu, L. Chang, C. Bai, L. Chen, R. Luque, Y. Li, Controllable encapsulation of "Clean" metal clusters within MOFs through kinetic modulation: towards advanced heterogeneous nanocatalysts, Angew. Chem. Int. Ed. 55 (2016) 5019–5023.

[35] H. Chen, K. Shen, J. Chen, X. Chen, Y. Li, Hollow-ZIF-templated formation of a $ZnO@$ C–N–Co core–shell nanostructure for highly efficient pollutant photodegradation, J. Mater. Chem. A 5 (2017) 9937–9945.

[36] J. Chen, J. Chen, Y. Li, Hollow ZnCdS dodecahedral cages for highly efficient visible-light-driven hydrogen generation, J. Mater. Chem. A 5 (2017) 24116–24125.

[37] H. Cheng, B. Huang, Y. Liu, Z. Wang, X. Qin, X. Zhang, Y. Dai, An anion exchange approach to Bi_2WO_6 hollow microspheres with efficient visible light photocatalytic reduction of CO_2 to methanol, Chem. Commun. 48 (2012) 9729–9731.

[38] D. Zheng, X.N. Cao, X. Wang, Precise formation of a hollow carbon nitride structure with a janus surface to promote water splitting by photoredox catalysis, Angew. Chem. Int. Ed. 55 (2016) 11512–11516.

[39] W. Tu, Y. Zhou, Q. Liu, Z. Tian, J. Gao, X. Chen, H. Zhang, J. Liu, Z. Zou, Robust hollow spheres consisting of alternating titania nanosheets and graphene nanosheets with high photocatalytic activity for CO_2 conversion into renewable fuels, Adv. Funct. Mater. 22 (2012) 1215–1221.

[40] J. Sun, J. Zhang, M. Zhang, M. Antonietti, X. Fu, X. Wang, Bioinspired hollow semiconductor nanospheres as photosynthetic nanoparticles, Nat. Commun. 3 (2012) 1139.

[41] W. Feng, Y. Feng, Z. Wu, A. Fujii, M. Ozaki, K. Yoshino, Optical and electrical characterizations of nanocomposite film of titania adsorbed onto oxidized multi-walled carbon nanotubes, J. Phys. Condens. Matter 17 (2005) 4361.

[42] W.J. Lee, J.M. Lee, S.T. Kochuveedu, T.H. Han, H.Y. Jeong, M. Park, J.M. Yun, J. Kwon, K. No, D.H. Kim, S.O. Kim, Biomineralized N-Doped CNT/TiO$_2$ Core/Shell nanowires for visible light photocatalysis, ACS Nano 6 (2012) 935–943.

[43] Y. Pi, X. Li, Q. Xia, J. Wu, Z. Li, Y. Li, J. Xiao, Formation of willow leaf-like structures composed of NH$_2$-MIL68(In) on a multifunctional multiwalled carbon nanotube backbone for enhanced photocatalytic reduction of Cr(VI), Nano Res. 10 (2017) 3543–3556.

[44] W. Cho, H.J. Lee, M. Oh, Growth-controlled formation of porous coordination polymer particles, J. Am. Chem. Soc. 130 (2008) 16943–16946.

[45] S. Goyanes, G. Rubiolo, A. Salazar, A. Jimeno, M. Corcuera, I. Mondragon, Carboxylation treatment of multiwalled carbon nanotubes monitored by infrared and ultraviolet spectroscopies and scanning probe microscopy, Diamond Relat. Mater. 16 (2007) 412–417.

[46] R. Wu, Y. Xu, R. Xu, Y. Huang, B. Zhang, Ultrathin-nanosheet-based 3D hierarchical porous In$_2$S$_3$ microspheres: chemical transformation synthesis, characterization, and enhanced photocatalytic and photoelectrochemical property, J. Mater. Chem. A 3 (2015) 1930–1934.

[47] X. Li, B. Weng, N. Zhang, Y.-J. Xu, In situ synthesis of hierarchical In$_2$S$_3$–graphene nanocomposite photocatalyst for selective oxidation, RSC Adv. 4 (2014) 64484–64493.

[48] C. Petit, J. Burress, T.J. Bandosz, The synthesis and characterization of copper-based metal–organic framework/graphite oxide composites, Carbon 49 (2011) 563–572.

[49] K.N. Kudin, B. Ozbas, H.C. Schniepp, R.K. Prud'homme, I.A. Aksay, R. Car, Raman Spectra of graphite oxide and functionalized graphene sheets, Nano Lett. 8 (2008) 36–41.

[50] W. Gao, W. Liu, Y. Leng, X. Wang, X. Wang, B. Hu, D. Yu, Y. Sang, H. Liu, In$_2$S$_3$ nanomaterial as a broadband spectrum photocatalyst to display significant activity, Appl. Catal. B Environ. 176 (2015) 83–90.

[51] W.-c. Peng, X. Wang, X.-y. Li, The synergetic effect of MoS$_2$ and graphene on Ag$_3$PO$_4$ for its ultra-enhanced photocatalytic activity in phenol degradation under visible light, Nanoscale 6 (2014) 8311–8317.

[52] J. Xu, X. Cao, Characterization and mechanism of MoS$_2$/CdS composite photocatalyst used for hydrogen production from water splitting under visible light, Chem. Eng. J. 260 (2015) 642–648.

[53] H. Wang, X. Yuan, Y. Wu, G. Zeng, X. Chen, L. Leng, H. Li, Synthesis and applications of novel graphitic carbon nitride/metal-organic frameworks mesoporous photocatalyst for dyes removal, Appl. Catal. B Environ. 174 (2015) 445–454.

[54] Z. Li, Z. Zhou, J. Ma, Y. Li, W. Peng, G. Zhang, F. Zhang, X. Fan, Hierarchical photocatalyst of In$_2$S$_3$ on exfoliated MoS$_2$ nanosheets for enhanced visible-light-driven Aza-Henry reaction, Appl. Catal. B Environ. (2018).

[55] T. Peng, P. Zeng, D. Ke, X. Liu, X. Zhang, Hydrothermal preparation of multiwalled carbon nanotubes (MWCNTs)/CdS nanocomposite and its efficient photocatalytic hydrogen production under visible light irradiation, Energy Fuels 25 (2011) 2203–2210.

[56] C. Tapia, S. Zacarias, I.A.C. Pereira, J.C. Conesa, M. Pita, A.L. De Lacey, In situ determination of photobioproduction of H$_2$ by In$_2$S$_3$-[NiFeSe] hydrogenase from Desulfovibrio vulgaris hildenborough using only visible light, ACS Catal. 6 (2016) 5691–5698.

[57] X. Li, Y. Pi, L. Wu, Q. Xia, J. Wu, Z. Li, J. Xiao, Facilitation of the visible light-induced Fenton-like excitation of H2O2 via heterojunction of g-C$_3$N$_4$/NH$_2$-Iron terephthalate metal-organic framework for MB degradation, Appl. Catal. B Environ. 202 (2017) 653–663.

[58] J. Chen, H. Zhang, P. Liu, Y. Li, X. Liu, G. Li, P.K. Wong, T. An, H. Zhao, Cross-linked ZnIn$_2$S$_4$/rGO composite photocatalyst for sunlight-driven photocatalytic degradation of 4-nitrophenol, Appl. Catal. B Environ. 168-169 (2015) 266–273.

[59] L. Jing, Y. Xu, S. Huang, M. Xie, M. He, H. Xu, H. Li, Q. Zhang, Novel magnetic CoFe$_2$O$_4$/Ag/Ag$_3$VO$_4$ composites: highly efficient visible light photocatalytic and antibacterial activity, Appl. Catal. B Environ. 199 (2016) 11–22.

[60] T. Zhu, H.B. Wu, Y. Wang, R. Xu, X.W. Lou, Formation of 1D hierarchical structures composed of Ni$_3$S$_2$ nanosheets on CNTs backbone for supercapacitors and photocatalytic H$_2$ production, Adv. Energy Mater. 2 (2012) 1497–1502.

[61] V. Spagnol, E. Sutter, C. Debiemme-Chouvy, H. Cachet, B. Baroux, EIS study of photo-induced modifications of nano-columnar TiO$_2$ films, Electrochim. Acta 54 (2009) 1228–1232.

[62] D.-S. Kong, The influence of fluoride on the physicochemical properties of anodic oxide films formed on titanium surfaces, Langmuir 24 (2008) 5324–5331.

[63] A. Ishikawa, T. Takata, J.N. Kondo, M. Hara, H. Kobayashi, K. Domen, Oxysulfide Sm$_2$Ti$_2$S$_2$O$_5$ as a Stable Photocatalyst for Water Oxidation and reduction under visible light irradiation ($\lambda \leq 650$ nm), J. Am. Chem. Soc. 124 (2002) 13547–13553.

[64] H. Shen, W. Xue, F. Fu, J. Sun, Y. Zhen, D. Wang, B. Shao, J. Tang, Efficient degradation of phenol and 4-Nitrophenol by surface oxygen vacancies and plasmonic silver Co-modified Bi2MoO6 photocatalysts, Chem. Eur. J. 24 (2018) 18463–18478.

[65] Z. Li, Y. Pi, D. Xu, Y. Li, W. Peng, G. Zhang, F. Zhang, X. Fan, Utilization of MoS$_2$ and graphene to enhance the photocatalytic activity of Cu$_2$O for oxidative CC bond formation, Appl. Catal. B Environ. 213 (2017) 1–8.